


## Nonlinear magnetoelectric effect in atomic vapor and its application to precision radio-frequency magnetometry

Sushree S. Sahoo <sup>1,2,3,\*</sup>, Soumya R. Mishra <sup>1,2</sup>, G. Rajalakshmi <sup>3</sup> and Ashok K. Mohapatra <sup>1,2,†</sup>

<sup>1</sup>National Institute of Science Education and Research Bhubaneswar, Jatni 752050, India

<sup>2</sup>Homi Bhabha National Institute, Training School Complex, Anushaktinagar, Mumbai 400094, India

<sup>3</sup>TIFR Centre for Interdisciplinary Sciences, Tata Institute of Fundamental Research, Hyderabad 500046, India



(Received 2 March 2022; accepted 25 May 2022; published 13 June 2022)

We demonstrate the nonlinear magnetoelectric (ME) effect in atomic vapor achieved through the parametric interaction of optical electric and radio-frequency (rf) magnetic fields leading to the generation of new optical electric fields. Density matrix calculations are performed to validate the experimental results. Moreover, the predicted dependence of the generated optical electric field amplitudes on the rf magnetic field strength is experimentally verified to confirm the ME effect. The system provides a technique for precision rf magnetometry based on this phenomenon. We could experimentally achieve an rf magnetic field sensitivity of  $70 \text{ fT}/\sqrt{\text{Hz}}$  at  $1 \text{ kHz}$  to  $7.5 \text{ pT}/\sqrt{\text{Hz}}$  at  $3 \text{ MHz}$  for zero bias field in an unshielded environment. The appealing features of the proposed rf magnetometer using our system include a high dynamic range up to  $10^{12}$ ,  $6 \text{ dB}$  bandwidth of  $450 \text{ kHz}$ , and arbitrary frequency resolution, which are intrinsic to the nonlinear ME effect in the medium.

DOI: [10.1103/PhysRevA.105.063509](https://doi.org/10.1103/PhysRevA.105.063509)

### I. INTRODUCTION

The magnetoelectric (ME) effect refers to the coupling between electric and magnetic fields in a medium resulting in electric polarization induced by magnetic fields and magnetization induced by electric fields. The electrical polarization due to the ME effect [1,2] induced in a medium in response to the applied electric field  $E$  and magnetic field  $B$ , is defined by the general expression

$$\begin{aligned}
 P_i(E, B) = & \chi_{ij}^{ee} E_j + \chi_{ij}^{em} B_j + \chi_{ijk}^{eee} E_j E_k + \chi_{ijk}^{emm} B_j B_k \\
 & + \chi_{ijk}^{em} E_j B_k + \chi_{ijkl}^{emmm} E_j B_k B_l + \\
 & + \chi_{ijkl}^{eeee} E_j E_k E_l \dots, \quad (1)
 \end{aligned}$$

where the indices  $ijk$  refer to the polarization components of the fields, whereas the indices  $e$  and  $m$  denote the electric and magnetic fields, respectively.  $\chi_{ij}^{ee}$  signifies the linear electric susceptibility,  $\chi_{ij}^{em}$  describes the linear ME effect, while the leading higher-order ME contributions are described by the tensors  $\chi_{ijk}^{emm}$ ,  $\chi_{ijk}^{em}$ , and  $\chi_{ijkl}^{emmm}$ . The terms  $\chi_{ijk}^{eee}$  and  $\chi_{ijkl}^{eeee}$  signify the higher-order electric susceptibilities due to the coupling of multiple electric fields. The linear as well as nonlinear ME effects in certain heterostructures such as multiferroics have drawn great interest due to their relevance in the fabrication of spintronics devices, memories, and magnetic sensors [3–11]. We explore the nonlinear ME effects manifested as the wave mixing of electric and magnetic fields in a simple system using atomic vapor. We specifically study the effect described by the polarization terms given by  $P_i^{(2)} = \chi_{ijk}^{em} E_j B_k$  and  $P_i^{(3)} = \chi_{ijkl}^{emmm} E_j B_k B_l$ . The polarization  $P_i^{(2)}$  is a

result of the mixing of three fields, i.e., two input fields (one electric and one magnetic field) and one generated electric field, whereas  $P_i^{(3)}$  results from the mixing of four fields, i.e., three input fields (one electric and two magnetic fields) and one generated electric field.

In the traditional nonlinear optics involving optical electric fields, the even-order electrical susceptibilities vanish (i.e.,  $P^{(2)} \propto \chi_{ijk}^{eee} E_j E_k = 0$ ) for a centrosymmetric medium such as atomic vapor. However, here we demonstrate nonvanishing even-order susceptibilities involving the coupling of electric and magnetic fields ( $\chi_{ijk}^{em} E_j B_k$ ) in atomic vapor. Thus, understanding this phenomenon would pave the way toward the investigation of fundamentally different nonlinear magneto-optical effects. An atomic system coupled to an optical electric field and an rf magnetic field which undergoes a wave-mixing process producing light at optical frequencies as satisfied by the energy conservation is studied here. The mixing between microwave and optical fields in atomic systems is an example of such mixing processes [12–14]. Moreover, we investigate the characteristic features of the generated optical electric fields such as the polarization, resonance width, and the variation of generated field amplitudes with input optical power.

This exploration of the nonlinear ME effect is of practical significance due to its potential application in precision rf magnetometry. The rf magnetic field-dependent optical signal in our system offers a conventionally different technique for rf magnetic field measurement. Previous works on rf magnetometry are based on atomic magnetometers or superconducting quantum interference devices (SQUIDs). The rf SQUIDs are less sensitive to their DC counterparts and give sensitivities of the order of  $30 \text{ fT}/\sqrt{\text{Hz}}$  at  $77 \text{ K}$  [15]. Atomic magnetometers measure the polarization rotation of an input linearly polarized beam in the presence of an rf magnetic field coupling the Zeeman sublevels of the ground state [16–24]. So far,

\*ssahoo@tifrh.res.in

†a.mohapatra@niser.ac.in

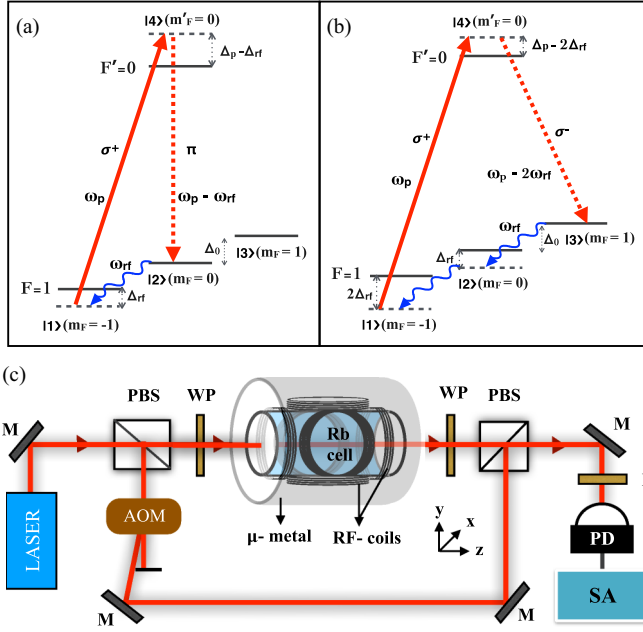


FIG. 1. Depiction of the (a) three-wave and (b) four-wave mixing processes in the schematic energy diagram for  $D_2$  line,  $^{87}\text{Rb}$   $F = 1 \rightarrow F = 0$  transition. Here, the input fields are the pump optical electric field ( $\omega_p$ ) and the rf magnetic field ( $\omega_{rf}$ ) leading to the optical electric field generation at frequencies  $\omega_p - \omega_{rf}$  via three-wave mixing and  $\omega_p - 2\omega_{rf}$  via four-wave mixing processes.  $\Delta_p$  ( $\Delta_{rf}$ ) is the detuning of the input optical (rf) field from the corresponding atomic transition. (c) Schematic of the experimental setup for the observation of the mixing process. PBS: polarizing beam splitter; M: mirror; AOM: acousto-optic modulator; WP: wave plate; P: polarizer; PD: photodetector; SA: spectrum analyzer.

the sensitivity reached with an atomic rf magnetometer is  $0.3 \text{ fT}/\sqrt{\text{Hz}}$  at  $0.5 \text{ MHz}$  in thermal vapor [21] and  $330 \text{ pT}/\sqrt{\text{Hz}}$  in the cold atomic ensemble [22]. To achieve the sensitivity below  $\text{fT}/\sqrt{\text{Hz}}$  as reported in Ref. [22], a shielding factor of  $10^6$  was used to maintain the uniform DC magnetic field in the vapor cell. In this work, we demonstrate an rf magnetic field sensitivity of  $70 \text{ fT}/\sqrt{\text{Hz}}$  at  $1 \text{ kHz}$  to  $7.5 \text{ pT}/\sqrt{\text{Hz}}$  at  $3 \text{ MHz}$  using the ME effect under ambient conditions and an unshielded environment. The system also inherently exhibits other attractive features such as a high dynamic range, a large bandwidth, as well as arbitrary frequency resolution.

## II. THEORETICAL MODEL

The schematic of the atomic energy levels coupled by the input optical electric field and rf magnetic field is shown in Figs. 1(a) and 1(b). The pump optical electric field with frequency  $\omega_p$  of right-handed circular ( $\sigma^+$ ) polarization, coupling the ground state with  $m_F = -1$  to the excited state with  $m'_F = 0$ , drives the population from  $m_F = -1$  to  $m_F = 0$  and  $m_F = 1$  ground states via optical pumping. There are two possible parametric cycles in the system. An atom present in the  $m_F = 0$  ground state emits one  $\sigma^+$  rf photon to come to the  $m_F = -1$  state, then absorbs the  $\sigma^+$  pump photon to be excited to the  $m'_F = 0$  state, and finally emits a linearly polarized ( $\pi$ ) optical photon to come back to the  $m_F = 0$  state. This parametric process is a three-wave mixing

process, which can be described by  $P_{\pi}^{(2)} (= \chi_{\pi\sigma^+\sigma^+}^{em} E_{\sigma^+} B_{\sigma^+}^*)$  as discussed before. Similarly, in the four-wave mixing process, the atom starting with the  $m_F = 1$  ground state emits two  $\sigma^+$  rf photons to come to the  $m'_F = -1$  state and absorbs one  $\sigma^+$  pump photon to be excited to the  $m'_F = 0$  state, and then comes back to the  $m_F = 1$  state by emitting a left-handed circularly polarized ( $\sigma^-$ ) optical photon. This four-wave mixing process is described by  $P_{\sigma^-}^{(3)} (= \chi_{\sigma^-\sigma^+\sigma^+\sigma^+}^{emmm} E_{\sigma^+} B_{\sigma^+}^{*2})$ . The energy conservation leads to optical electric field generation at frequencies  $\omega_{g1} (= \omega_p - \omega_{rf})$  and  $\omega_{g2} (= \omega_p - 2\omega_{rf})$  via three-wave mixing and four-wave mixing processes, respectively. The polarization states of the generated optical electric fields are decided by the angular momentum conservation in both of the processes, i.e., for an input  $\sigma^+$  polarized pump beam, the three-wave mixing process leads to a generated beam with linear ( $\pi$ ) polarization, whereas the four-wave mixing process leads to a generated beam with  $\sigma^-$  polarization. Furthermore, as the wave vector of the rf magnetic field is negligible compared to that of the optical electric field, the phase-matching conditions ensure that the direction of the generated beams is the same as that of the input pump beam.

To theoretically model the system, we consider the atomic system as shown in Figs. 1(a) and 1(b). The Hamiltonian of the system in the rotating frame under electric and magnetic dipole approximation is given by the expression

$$H = -\hbar[\Delta_{rf}(|1\rangle\langle 1| - |3\rangle\langle 3|) + (\Delta_p + \Delta_{rf})|4\rangle\langle 4| + \Omega_{rf}(|1\rangle\langle 2| + |2\rangle\langle 3|) + \Omega_p|4\rangle\langle 1| + \text{H.c.}] \quad (2)$$

Here,  $\Omega_p (= \frac{\mu_{41} E_p}{\hbar})$  and  $\Omega_{rf} (= \frac{\mu_m B_{rf}}{\hbar})$  are the Rabi frequencies of the input pump optical electric field and the rf magnetic field, respectively.  $\mu_{41}$  and  $\mu_m = \mu_{21} = \mu_{32}$  are the electric and magnetic transition dipole moment of the corresponding atomic levels. The time evolution of the system is described by the optical Bloch equation  $\frac{d\rho}{dt} = -\frac{i}{\hbar}[H, \rho] + \mathcal{L}_D$ . Here,  $\mathcal{L}_D$  describes the decay and dephasing mechanisms present in the system, which includes the population decay rate ( $\Gamma$ ) from the excited state to the ground states and the dipole-dephasing rate ( $\gamma$ ) associated with the ground states. The equations are solved for the steady-state condition to evaluate the analytical expressions for  $\rho_{42}$  and  $\rho_{43}$ , which give information about the generated optical electric field amplitudes via three- and four-wave mixing processes, respectively. Here, we have neglected the population in the excited state, i.e.,  $\rho_{44} = 0$  as  $\Delta_p \gg \Omega_p$ ,  $\Gamma$ ,  $\gamma$ ,  $\Delta_{rf}$ . If  $\Omega_p \gg \Omega_{rf}$ , then the optical pumping process results in  $\rho_{11} = 0$  and  $\rho_{22} = \rho_{33} = 0.5$ . Using these approximations, the susceptibilities corresponding to  $\omega_{g1}$  and  $\omega_{g2}$  with the respective Rabi frequencies  $\Omega_{g1}$  and  $\Omega_{g2}$  are given by

$$\chi_{(g1)}^{em} = \frac{N\mu_{42}\mu_{41}\mu_m}{2\epsilon_0\hbar^2\Delta_1\Delta_2} \left( \frac{c_2\Delta_2 + c_0\Omega_{rf}^2}{c_1c_2 - c_0^2\Omega_{rf}^2} \right), \quad (3)$$

$$\chi_{(g2)}^{emmm} = \frac{N\mu_{43}\mu_{41}\mu_m^2}{2\epsilon_0\hbar^3\Delta_1\Delta_2} \left( \frac{c_1 + c_0\Delta_2}{c_0^2\Omega_{rf}^2 - c_1c_2} \right). \quad (4)$$

Here,  $\Delta_1 = \Delta_{rf} + i\gamma$ ,  $\Delta_2 = 2\Delta_{rf} + i\gamma$ ,  $c_0 = 1 + \frac{\Omega_p^2}{2\Delta_1\Delta_2}$ ,  $c_1 = \Delta_p - \frac{\Omega_p^2}{\Delta_1}$ , and  $c_2 = \Delta_p - \frac{\Omega_p^2}{\Delta_2}$ .  $N$  is the number density of the atoms, whereas  $\mu_{42}$  and  $\mu_{43}$  are the electric dipole moment of the corresponding atomic transitions. Equations (3) and

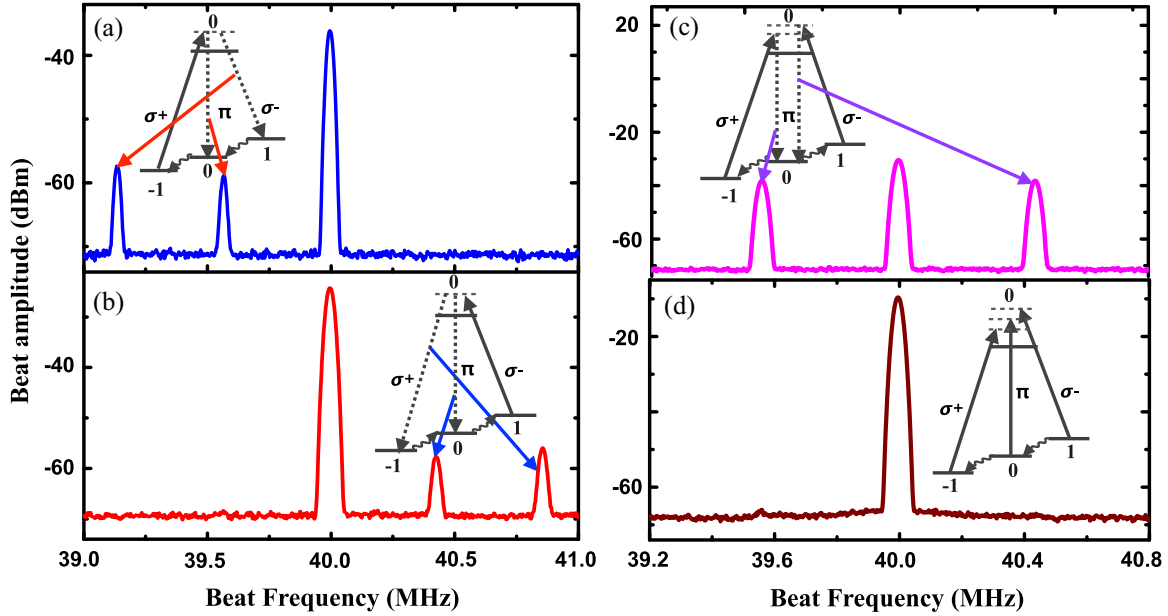


FIG. 2. Experimental data of the generated beat amplitudes when the input pump beam is (a)  $\sigma^+$  polarized, (b)  $\sigma^-$  polarized, (c) linearly polarized with equal components of  $\sigma^+$  and  $\sigma^-$  polarization ( $\frac{1}{\sqrt{2}}(\sigma^+ + \sigma^-)$ ), and (d) linearly polarized with equal components of all  $\sigma^+$ ,  $\sigma^-$ , and  $\pi$  polarizations. The larger peak at 40 MHz refers to the beat note corresponding to the interference of the LO and the input pump light. The other peaks correspond to the generated optical electric fields which appear exactly at  $\omega_p \pm \omega_{rf}$  and  $\omega_p \pm 2\omega_{rf}$  and are indicated by the inset showing the respective wave-mixing processes in the energy-level diagrams. Here, the input pump power at the entrance of the cell is  $10 \mu\text{W}$  ( $\Omega_p = 1.8 \text{ MHz}$ ) while the pump beam waist is 1.5 mm.

(4) provide information about the generated optical electric field amplitudes due to the three-wave mixing and four-wave mixing processes, respectively.

### III. EXPERIMENTAL METHODS

The schematic of the experimental setup is depicted in Fig 1(c). The pump beam, derived from an external cavity diode laser (tuned to 780 nm), is split into two parts, where one beam is directed to a rubidium vapor cell of length 5 cm and the other part is shifted using AOMs by 40 MHz to be used as a local oscillator (LO). We use a  $\lambda/4$  ( $\lambda/2$ ) plate to make the input pump beam circularly (linearly) polarized before the cell and another  $\lambda/4$  ( $\lambda/2$ ) plate to convert it back to a linear (orthogonal linear) polarization after the cell. As the optical electric fields are generated along the same direction as the input pump beam, all the output beams are combined with the LO reference beam using a polarizing beam splitter for heterodyne detection. This combined output light is then passed through a polarizer and collected in a photodetector (APD120A, Thorlabs) to be analyzed in a spectrum analyzer (N9000A CXA Signal Analyser, Agilent). The wave-mixing processes are found to be efficient for larger population differences between the ground-state Zeeman sublevels. Also, in a Doppler broadened atomic vapor, there is a trade-off between the efficiency of the nonlinear mixing process and absorption in the medium. The generation of light due to mixing is optimized when the laser beam is red detuned by 300 MHz to the  $^5S_{1/2} F = 1 \rightarrow ^5P_{3/2} F = 0$  transition of  $^{87}\text{Rb}$  to create a larger population difference between the Zeeman sublevels through optical pumping with reduced absorption. The vapor

cell is enclosed with three layers of  $\mu$ -metal sheets to shield the effect of stray magnetic fields. Furthermore, the cell is heated up to  $80^\circ\text{C}$ , which corresponds to an atomic vapor density of  $1.8 \times 10^{12} \text{ cm}^{-3}$ . We use three pairs of Helmholtz coils to apply the magnetic field along the  $x$ ,  $y$ , and  $z$  directions.

### IV. RESULTS AND DISCUSSION

In the first experiment, we apply a static magnetic field along the  $z$  direction to define the quantization axis and to split the Zeeman sublevels of the ground state. In this way, the pump polarization is always perpendicular to the dc magnetic field and hence can be made  $\sigma^+$  or  $\sigma^-$  polarized using the input  $\lambda/4$  plate. In this experiment, we apply the rf magnetic field in the  $y$  coil with its frequency matching the Zeeman splitting. The experimental data for the input circularly polarized light are presented in Figs. 2(a) and 2(b). As expected, when we use the pump with  $\sigma^+$  ( $\sigma^-$ ) circular polarization, the optical electric fields due to the mixing process are generated with lower (higher) optical frequencies than the pump optical field and hence the interference peak with LO appears at the left (right) side of the main peak. It is interesting to note that this frequency up or down conversion process is a direct method to determine the handedness of circular polarization of light interacting with the medium.

In a further experiment, the static and rf magnetic fields are applied along the  $y$  and  $z$  directions, respectively. It leads to the realization of any arbitrary linear polarization for the pump beam of the form  $c_1|\pi\rangle + c_2|\sigma^+\rangle + c_3|\sigma^-\rangle$ , where  $c_1$ ,  $c_2$ , and  $c_3$  are controlled using the input  $\lambda/2$  plate. When the polarization of the input pump optical electric field is a linear combination of  $\sigma^+$  and  $\sigma^-$  polarizations, i.e., of the form

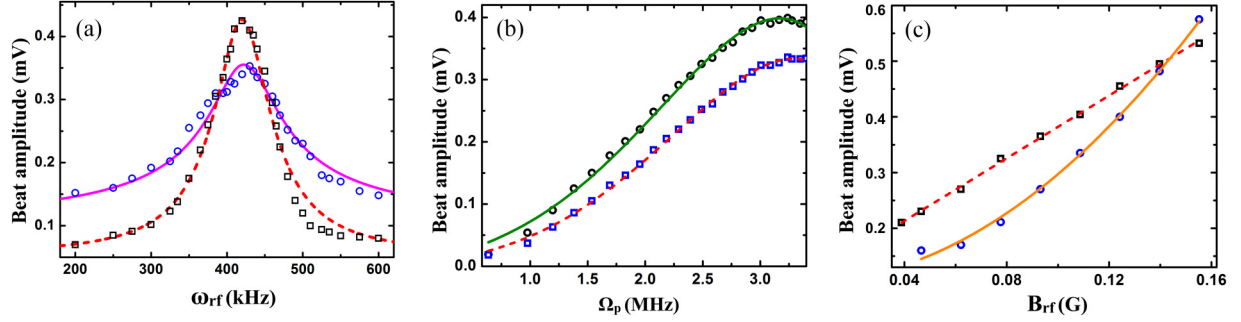


FIG. 3. (a) Resonance curves corresponding to the generated beat signals as a variation of the input rf frequency ( $\omega_{rf}$ ). Here, blue open circles (black open squares) depict the experimental data, and the magenta solid line (dashed red line) depicts the theoretical fitting corresponding to the generated optical electric field  $\omega_{g1}$  ( $\omega_{g2}$ ). The input parameters for the model are  $\Omega_p = 0.5$  MHz,  $\Omega_{rf} = 80$  kHz,  $\Delta_p = 150$  MHz,  $\Gamma = 6$  MHz, and  $\Delta_0 = 425$  kHz, whereas the fitting parameter is  $\gamma = 65$  kHz. Here, the amplitude of the rf magnetic field used is 57 mG, while the static magnetic field strength along the  $z$  direction is 0.6 G. The input pump power at the entrance of the cell is  $10 \mu\text{W}$  ( $\Omega_p = 1.8$  MHz). (b) Variation of the generated beat amplitudes at resonance of the data shown in (a) as a variation of the input pump Rabi frequency ( $\Omega_p$ ). The black open circles (blue open squares) depict the experimental data and the green solid line (dashed red line) shows the theoretical fitting corresponding to  $\omega_{g1}$  ( $\omega_{g2}$ ). Here, the fitting function is of the form  $a_i\Omega_p + b_i\Omega_p^3 + c_i\Omega_p^5$ , with the fitting parameters given as  $a_1(a_2) = 31.7 \pm 1.9$  ( $52.4 \pm 3.5$ ) mV/MHz,  $b_1(b_2) = 17.5 \pm 0.6$  ( $20.9 \pm 1.1$ ) mV/MHz<sup>3</sup>, and  $c_1(c_2) = -1.0 \pm 0.1$  ( $-1.4 \pm 0.1$ ) mV/MHz<sup>5</sup> for the  $\omega_{g1}$  ( $\omega_{g2}$ ) signal. (c) Variation of beat amplitudes of the generated optical electric fields with the amplitude of the rf magnetic field ( $B_{rf}$ ) showing linear (black open squares) and quadratic (blue open circles) behavior for the  $\omega_{g1}$  and  $\omega_{g2}$  signals, respectively. Fittings of both of the data correspond to a common offset of  $10 \mu\text{V}$  at zero input rf field strength, which is mostly due to the presence of rf magnetic field noise and the photodetector noise in the system. The frequency of the rf magnetic field in this case is 300 kHz, while the strength of the static magnetic field along the  $z$  direction is 0.43 G.

$\frac{1}{\sqrt{2}}(|\sigma^+\rangle + |\sigma^-\rangle)$ , both of the generated optical electric fields in this case are  $\pi$  polarized with optical frequencies  $\omega_p + \omega_{rf}$  and  $\omega_p - \omega_{rf}$ . The respective experimental data for the beat amplitudes are presented in Fig. 2(c). On the other hand, when the input pump is  $\pi$  polarized, the generated beams are observed to be  $\sigma^+$  ( $\omega_p + \omega_{rf}$ ) and  $\sigma^-$  ( $\omega_p - \omega_{rf}$ ) polarized. Furthermore, when the input linear polarization is such that it has equal components of  $\sigma^+$ ,  $\sigma^-$ , and  $\pi$  polarizations, all the ground states become equally populated, leading to no generation due to mixing. In this case, the ground-state coherence, which is responsible for the efficient mixing process, is no longer induced in the system as it requires a nonzero population difference between the Zeeman sublevels. It leads to the vanishing beat amplitudes for the generated optical electric fields, as depicted in Fig. 2(d).

The mixing process and hence the light generation is the most efficient when the frequency of the rf magnetic field ( $\omega_{rf}$ ) matches the Zeeman splitting ( $\Delta_0$ ). In the experiment, the rf magnetic field ( $\omega_{rf}$ ) is scanned around the Zeeman splitting to observe the resonance curves for both  $\omega_{g1}$  and  $\omega_{g2}$  for the case of the circularly polarized input pump beam. Figure 3(a) shows the experimental data for the resonance curves peaked at 425 kHz. We use the expression of  $\chi_{(g1)}^{eem}$  and  $\chi_{(g2)}^{eemm}$  from the theoretical model [Eqs. (3) and (4)] to fit the experimental data. From the fitting, we find the value of  $\gamma$  to be 65 kHz, which is the dephasing rate and is mostly dominated by the transit time of the atoms through the laser beams and the magnetic inhomogeneity present in the medium.

We also study the beat amplitude of the generated beams by varying the input pump Rabi frequency ( $\Omega_p$ ), and the experimental data for both  $\omega_{g1}$  and  $\omega_{g2}$  are presented in Fig. 3(b). To model this experimental observation, we consider the propagation equation for the generated optical electric field with

Rabi frequency  $\Omega_{gi}$  ( $i = 1, 2$ ), which can be written as

$$\frac{d\Omega_{gi}}{dz} = -\alpha_{gi}\Omega_{gi} + \kappa_{gi}, \quad (5)$$

where  $\alpha_{gi} = \frac{k_{gi}}{2} \text{Im}(\chi_{\text{eff}})$  corresponds to the gain or absorption in the medium, whereas  $\kappa_{g1} = i \frac{\hbar}{\mu_m} k_{g1} \chi_{(g1)}^{eem} \Omega_p \Omega_{rf}$  and  $\kappa_{g2} = i \frac{\hbar^2}{\mu_m^2} k_{g2} \chi_{(g2)}^{eemm} \Omega_p \Omega_{rf}^2$ , where  $k_{g1}$  and  $k_{g2}$  are the magnitude of the wave vectors corresponding to the generated optical electric fields  $\Omega_{g1}$  and  $\Omega_{g2}$ , respectively. This equation can be solved using the initial condition  $\Omega_{gi} = 0$  at  $z = 0$  to get

$$\Omega_{gi} = \frac{\kappa_{gi}}{\alpha_{gi}} (1 - e^{-\alpha_{gi}l}), \quad (6)$$

where  $l$  is the length of the vapor cell. By using the linear dependence of  $\kappa_{gi}$  with  $\Omega_p$ , expanding  $e^{-\alpha_{gi}l}$  to second order under the assumption of  $\alpha_{gi}l \ll 1$ , and using  $\alpha_{gi} = \alpha_0 + \alpha_1\Omega_p^2 + \alpha_2\Omega_p^4$  with  $\alpha_0$ ,  $\alpha_1$ , and  $\alpha_2$  being the absorption coefficients corresponding to the linear and nonlinear processes, the expression for  $\Omega_{gi}$  can be simplified to a polynomial of odd orders of  $\Omega_p$ . The photodetector signal of the generated beat amplitudes is proportional to  $\Omega_{gi}$  and can be expressed as

$$S_{Di} = q_i \Omega_{gi} = a_i \Omega_p + b_i \Omega_p^3 + c_i \Omega_p^5. \quad (7)$$

Here,  $q_i$  takes care of the overall gain of the heterodyne detection of the generated field. The coefficients are given as

$$a_1 = q_1 \frac{i\hbar}{\mu_m} k_{g1} \chi_{(g1)}^{eem} \Omega_{rf} l \left(1 - \frac{\alpha_0 l}{2}\right),$$

$$b_1 = -q_1 \frac{i\hbar}{\mu_m} k_{g1} \chi_{(g1)}^{eem} \Omega_{rf} \frac{\alpha_1 l^2}{2},$$

$$c_1 = -q_1 \frac{i\hbar}{\mu_m} k_{g1} \chi_{(g1)}^{eem} \Omega_{rf} \frac{\alpha_2 l^2}{2},$$

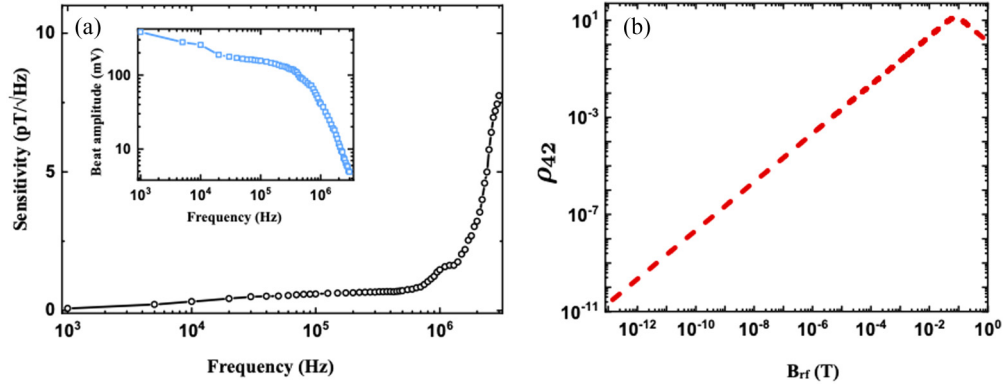


FIG. 4. (a) The magnetic field sensitivity of the system is shown by the black open circles. Inset: Variation of the beat signal amplitude of the generated beams for different rf frequencies (blue squares), which shows the beat amplitude of 380 mV corresponding to 100 nT of the rf field at 1 kHz. The solid lines are guides to the eye. (b) Theoretical plot of  $\rho_{42}$  as a function of the rf magnetic field (red dashed line) showing the dynamic range of the system to be  $\sim 10^{12}$ .

$$\begin{aligned}
 a_2 &= q_2 \frac{i\hbar^2}{\mu_m^2} k_{g2} \chi_{(g2)}^{eemm} \Omega_{rf}^2 l \left(1 - \frac{\alpha_0 l}{2}\right), \\
 b_2 &= -q_2 \frac{i\hbar^2}{\mu_m^2} k_{g2} \chi_{(g2)}^{eemm} \Omega_{rf}^2 \frac{\alpha_1 l^2}{2}, \\
 c_2 &= -q_2 \frac{i\hbar^2}{\mu_m^2} k_{g2} \chi_{(g2)}^{eemm} \Omega_{rf}^2 \frac{\alpha_2 l^2}{2}.
 \end{aligned} \quad (8)$$

We use the functional form as shown in Eq. (7) to fit the experimental data as shown in Fig. 3(b), which shows a good matching between the model and the experiment.

Furthermore, using  $\kappa_{g1} \propto \Omega_{rf}$  and  $\kappa_{g2} \propto \Omega_{rf}^2$  in Eq. (6) results in the linear (quadratic) dependence of the generated field,  $\Omega_{g1}(\Omega_{g2})$ , on the input rf magnetic field amplitude ( $B_{rf}$ ). To verify this dependence, we experimentally measured the generated beat amplitudes as a function of  $B_{rf}$ . The corresponding experimental data with linear and quadratic fittings are presented in Fig. 3(c). This experimental observation is a further confirmation of the nonlinear mixing between the optical electric field and the rf magnetic field occurring in the system. Moreover, this rf magnetic field-dependent signal can directly lead to applications in rf magnetometry.

## V. rf-MAGNETOMETRY WITH ME EFFECT

To have an estimate of the rf magnetic field sensitivity in our system, we consider the case of an input linearly polarized light with frequency  $\omega_p$ , such that we generate optical electric fields at frequencies  $\omega_p + \omega_{rf}$  and  $\omega_p - \omega_{rf}$  due to the ME effect [refer to Fig. 2(c)]. We measure the beat amplitude as a result of the interference of the generated fields with the pump beam rather than with the reference beam as used in previous measurements. This leads to a two-times increase in the signal amplitude at frequency  $\omega_{rf}$  due to the contribution from both of the beat signals. Moreover, the inherent spatial mode matching between the pump and the generated fields due to the wave-mixing processes leads to a larger amplitude of the beat signal. This measurement is performed without any static magnetic field in the transverse coil as it leads to a multifold enhancement in the optical generation. In this case, the optical generation is efficient for the lower frequency

of the rf field, whereas the amplitude of the generated field reduces with increasing frequency of the rf field, as shown by the blue squares in the inset of Fig. 4(a).

For an input rf magnetic field ( $B_{rf}$ ), we experimentally measured the signal-to-noise ratio (SNR) of the system with the noise expressed per unit bandwidth, and calculated the rf magnetic field sensitivity ( $\delta B$ ) using

$$\delta B = \frac{B_{rf}}{\text{SNR}}. \quad (9)$$

We present the experimental data for  $\delta B$  with a variation of the rf frequencies in Fig. 4(a). We use a higher optical power of the input pump field, i.e., in the saturation region of Fig. 3(b), to get the sensitivity. We could achieve the best sensitivity at the zero bias field given as  $70 \text{ fT}/\sqrt{\text{Hz}}$  for 1 kHz, whereas the sensitivity obtained at 3 MHz is found to be  $7.5 \text{ pT}/\sqrt{\text{Hz}}$ . On the other hand, in the presence of a finite static magnetic field, the resonance curve in the signal implies a better sensitivity at the Zeeman resonance frequency. The normalized beat signal amplitude, as presented in the inset of Fig. 4(a), shows the 3 dB bandwidth of our system to be 20 kHz, whereas the 6 dB bandwidth is given as 450 kHz. Here, the shape of the signal at a lower frequency, i.e., below 30 kHz, could be due to the contribution from multiple phenomena and its investigation is one of our future research interests [25]. The sensitivity and bandwidth measurements are done for an unshielded environment, and another set of Helmholtz coil pairs along the  $x$ ,  $y$ , and  $z$  directions are used for compensation of stray magnetic fields.

We have also estimated the dynamic range of the system using our theoretical model since, in the current experimental setup, we could provide the maximum input rf magnetic field ( $B_{rf}$ ) of  $\simeq 30 \mu\text{T}$  and did not observe any turning point in the beat signal. This is restricted by the current source and the coils we are presently using in our setup. The theoretical plot of the variation in  $\rho_{42}$  with rf magnetic field strength is presented in Fig. 4(b). The turning point in the plot is a consequence of the higher-order nonlinear processes in the system, which are significant at a higher amplitude of the rf magnetic field leading to a decrease in the amplitude of the generated fields. As our theoretical model provides an exact solution for the arbitrary magnitude of the rf magnetic field,

it takes account of these higher-order nonlinear processes. Figure 4(b) shows a turning point at  $\sim 80$  mT, which along with the current sensitivity of  $70 \text{ fT}/\sqrt{\text{Hz}}$ , corresponds to the dynamic range of  $\sim 10^{12}$ . This is better than the recent demonstration of an ultrahigh dynamic range of quantum sensors [26]. Another interesting feature of the proposed rf magnetometer using our system is its arbitrary resolution in frequency. Due to the parametric nature of the processes, the relative frequency noise between the input pump and the generated fields is limited by the frequency noise of the rf magnetic field. Now, in the context of rf magnetometry, the frequency of an unknown rf magnetic field can be measured from the interference beat signal of the input pump and the generated fields with a frequency resolution, which would be limited by the measurement devices. Therefore, the system has the potential to surpass the state-of-the-art frequency resolution of millihertz in a magnetometer [27].

## VI. CONCLUSION

The significance of this work is twofold: first, it would open up the possibility of an area of nonlinear magneto-optical

phenomena involving the coupling between electric and magnetic fields using an atomic system. Second, it can be used for precision rf magnetometry owing to the coexistence of many interesting features such as the simplicity of the setup, higher dynamic range, large bandwidth, and arbitrary frequency resolution, which make this system ideal for numerous applications such as sensing biological magnetic fields [28–30], detection of signals in magnetic resonance imaging (MRI) and nuclear magnetic resonance (NMR) [16,31–34], investigation of geomagnetic fields [35,36], measurement of the magnetic fields in space as well as for the search of dark matter [37–39], and, in general, for the application of sensitive magnetometry in different challenging environments [40].

## ACKNOWLEDGMENTS

The authors gratefully acknowledge the financial support from the Department of Atomic Energy, Government of India under the Project Identification No. XII-R&D-5.02-0200 (National Institute of Science Education and Research Bhubaneswar) and Project Identification No. RTI 4007 (Tata Institute of Fundamental Research Hyderabad).

- 
- [1] T. H. O’Dell, *The Electrostatics of Magneto-Electric Media* (North-Holland, Amsterdam, 1970).
- [2] M. Fiebig, *J. Phys. D: Appl. Phys.* **38**, R123 (2005).
- [3] Y. Tokura, *J. Magn. Magn. Mater.* **310**, 1145 (2007).
- [4] W. Kleemann, *J. Appl. Phys.* **114**, 027013 (2013).
- [5] J. F. Scott, *Nat. Mater.* **6**, 256 (2007).
- [6] M. Bibes and A. Barthélemy, *Nat. Mater.* **7**, 425 (2008).
- [7] N. A. Spaldin and R. Ramesh, *Nat. Mater.* **18**, 203 (2019).
- [8] D. A. Filippov, V. M. Laletin, and T. O. Firsova, *Phys. Solid State* **56**, 980 (2014).
- [9] J. Shen, J. Cong, Y. Chai, D. Shang, S. Shen, K. Zhai, Y. Tian, and Y. Sun, *Phys. Rev. Appl.* **6**, 021001(R) (2016).
- [10] L. Y. Fetisov *et al.*, *J. Phys. D: Appl. Phys.* **51**, 154003 (2018).
- [11] D. A. Burdin, N. A. Ekonomov, D. V. Chashin, Y. K. Fetisov, and S. N. Gordeev, *J. Magn. Magn. Mater.* **485**, 36 (2019).
- [12] A. S. Zibrov, A. B. Matsko, and M. O. Scully, *Phys. Rev. Lett.* **89**, 103601 (2002).
- [13] L. A. Williamson, Y.-H. Chen, and J. J. Longdell, *Phys. Rev. Lett.* **113**, 203601 (2014).
- [14] K. V. Adwaith, A. Karigowda, C. Manwatkar, F. Bretenakar, and A. Narayanan, *Opt. Lett.* **44**, 33 (2019).
- [15] Y. Zhang, M. Gottschlich, H. Soltner, E. Södtker, J. Schubert, W. Zander, and A. I. Braginski, *Appl. Phys. Lett.* **67**, 3183 (1995).
- [16] I. M. Savukov, S. J. Seltzer, M. V. Romalis, and K. L. Sauer, *Phys. Rev. Lett.* **95**, 063004 (2005).
- [17] S.-K. Lee, S.-K. Lee, S. J. Seltzer, O. Alem, and M. V. Romalis, *Appl. Phys. Lett.* **89**, 214106 (2006).
- [18] M. P. Ledbetter, V. M. Acosta, S. M. Rochester, D. Budker, S. Pustelny, and V. V. Yashchuk, *Phys. Rev. A* **75**, 023405 (2007).
- [19] T. Zigdon, A. D. Wilson-Gordon, S. Guttikonda, E. J. Bahr, O. Neitzke, S. M. Rochester, and D. Budker, *Opt. Express* **18**, 25494 (2010).
- [20] W. Chalupczak, R. M. Godun, S. Pustelny, and W. Gawlik, *Appl. Phys. Lett.* **100**, 242401 (2012).
- [21] D. A. Keder, D. W. Prescott, A. W. Conovaloff, and K. L. Sauer, *AIP Adv.* **4**, 127159 (2014).
- [22] Y. Cohen, K. Jadeja, S. Sula, M. Venturelli, C. Deans, L. Marmugi, and F. Renzoni, *Appl. Phys. Lett.* **114**, 073505 (2019).
- [23] A. M. Akulshin, R. J. McLean, A. I. Sidorov, and P. Hannaford, *J. Phys. B: At. Mol. Opt. Phys.* **44**, 175502 (2011).
- [24] D. Budker and M. Romalis, *Nat. Phys.* **3**, 227 (2007).
- [25] S. S. Sahoo, A. Bhowmick, and A. K. Mohapatra, *J. Phys. B: At. Mol. Opt. Phys.* **50**, 055501 (2017).
- [26] E. D. Herbschleb, H. Kato, T. Makino, S. Yamasaki, and N. Mizuochi, *Nat. Commun.* **12**, 306 (2021).
- [27] K. Mizuno, M. Nakajima, H. Ishiwata, Y. Masuyama, T. Iwasaki, and M. Hatano, *AIP Adv.* **8**, 125316 (2018).
- [28] Amir Borna, R. C. Tony, D. G. Josh, P. C. Anthony, J. Yuan-Yu, B. Christopher, M. Jim, S. Julia, W. Michael, and D. D. S. Peter, *Phys. Med. Biol.* **62**, 8909 (2017).
- [29] K. Jensen, M. A. Skarsfeldt, H. Starkind, J. Arnbak, M. V. Balabas, S.-P. Olesen, B. H. Bentzenand, and E. S. Polzik, *Sci. Rep.* **8**, 16218 (2018).
- [30] E. Boto, N. Holmes, J. Leggett, G. Roberts, V. K. Shah, S. S. Meyer, L. D. Muñoz, K. J. Mullinger, T. M. Tierney, S. Bestmann, G. R. Barnes, R. Bowtell, and M. J. Brookes, *Nature (London)* **555**, 657 (2018).
- [31] S. Xu, S. M. Rochester, V. V. Yashchuk, M. H. Donaldson, and D. Budker, *Rev. Sci. Instrum.* **77**, 083106 (2006).
- [32] I. M. Savukov, S. J. Seltzer, and M. V. Romalis, *J. Magn. Reson.* **185**, 214 (2007).
- [33] M. P. Ledbetter, C. W. Crawford, A. Pines, D. E. Wemmerb, S. Knappe, J. Kitching, and D. Budker, *J. Magn. Reson.* **199**, 25 (2009).
- [34] I. M. Savukov, Jr., V. S. Zotev, P. L. Volegov, M. A. Espy, A. N. Matlashov, J. J. Gomez, and R. H. Kraus Jr., *J. Magn. Reson.* **199**, 188 (2009).

- [35] H. B. Dang, A. C. Maloof, and M. V. Romalis, *Appl. Phys. Lett.* **97**, 151110 (2010).
- [36] M. N. Nabighian, V. J. S. Grauch, R. O. Hansen, T. R. LaFehr, Y. Li, J. W. Peirce, J. D. Phillips, and M. E. Ruder, *Geophysics* **70**, 33ND (2005).
- [37] C. T. Hill, *Phys. Rev. D* **93**, 025007 (2016).
- [38] S. Alexander and R. Sims, *Phys. Rev. D* **98**, 015011 (2018).
- [39] P.-H. Chu, Y. J. Kim, and I. Savukov, *Phys. Rev. D* **99**, 075031 (2019).
- [40] K.-M. C. Fu, G. Z. Iwata, A. Wickenbrock, and D. Budker, *AVS Quantum Sci.* **2**, 044702 (2020).